crystals

MDPI

Article

Frustrated Magnetism and Ferroelectricity in a Dy^{3+}-Based Triangular Lattice

Xianghan Xu [1], Choongjae Won [2,3] and Sang-Wook Cheong [1,2,*]

[1] Department of Physics and Astronomy, Rutgers University, Piscataway, NJ 08854, USA; xx80@physics.rutgers.edu
[2] Laboratory for Pohang Emergent Materials, Department of Physics, Pohang University of Science and Technology, Pohang 37673, Republic of Korea; cjwon@mpk.or.kr
[3] Max Planck POSTECH Center for Complex Phase Materials, Department of Physics, Pohang University of Science and Technology, Pohang 37673, Republic of Korea
* Correspondence: sangc@physics.rutgers.edu

Abstract: Triangular lattice magnets have attracted extensive research interest because they are potential hosts for geometrically frustrated magnetism and strong quantum fluctuations. Here, utilizing a laser floating zone technique, we report the first-time successful growth of a $DyInO_3$ sizable crystal, which contains Dy^{3+}-based triangular layers. The fine-tuning of Indium stoichiometry was found to be the key factor in the stabilization of the desired hexagonal phase. The X-ray diffraction study of the crystal structure reveals a non-centrosymmetric $P6_3mc$ space group. Switchable polarization, i.e., ferroelectricity, and ferroelectric domain configuration are experimentally demonstrated at room temperature. Anisotropic magnetic and thermodynamic measurements unveil antiferromagnetic interactions, the absence of long-range ordering down to 0.1 K, and a possible doublet ground state, indicating a strongly frustrated magnetism. Our findings suggest that the $DyInO_3$ crystal is an excellent platform for studying emergent phenomena and their interplay with coherent topological defects in the quantum realm.

Keywords: floating zone; ferroelectricity; triangular lattice; frustrated magnet; heat capacity

Citation: Xu, X.; Won, C.; Cheong, S.-W. Frustrated Magnetism and Ferroelectricity in a Dy^{3+}-Based Triangular Lattice. *Crystals* **2023**, *13*, 971. https://doi.org/10.3390/cryst13060971

Academic Editors: Artem Pronin and Xueyun Wang

Received: 17 May 2023
Revised: 10 June 2023
Accepted: 14 June 2023
Published: 19 June 2023

1. Introduction

The ABO_3 perovskite family holds a rich structural variety. It adopts an undistorted cubic structure when the Goldschmidt tolerance factor (t) is near 1, and alternative structures that are orthorhombic, rhombohedral, and hexagonal have been discovered, with t deviating from 1 [1,2]. Recently, the hexagonal ABO_3 has attracted growing research interest due to the discovery of emergent phenomena that facilitate the understanding of fundamental physics as well as advanced technology applications. For example, a strongly correlated quantum spin liquid (QSL) ground state has been experimentally demonstrated in hexagonal $TbInO_3$ with effective S = 1/2 Tb^{3+}-based triangular lattices [3–5]. Moreover, improper ferroelectricity arising from a trimerization-type structural phase transition has been extensively studied in the hexagonal $REMnO_3$, and this structural transition leads to three structural domains, each of which can support two directions of ferroelectric polarization, giving rise to a cloverleaf arrangement that cycles through all six domain configurations, i.e., a structural Z_3 topological defect [6–9], which provides opportunities for functional domain wall engineering [10,11]. On the other hand, because the tolerance factor is substantially lower than 1 and because of the significantly distorted non-centrosymmetric lattice, the crystal growth of hexagonal ABO_3 is generally tricky, and the crystal's quality, ferroelectric behaviors, and domain configurations strongly depend on the choice of growth and annealing parameters [12].

Here, we report the growth of a sizable $DyInO_3$ single crystal for the first time utilizing a laser floating zone (LFZ) technique. The fine-tuning of the growth parameters reveals that

the precise control of In_2O_3 stoichiometry in the molten zone is the key factor for obtaining high-quality $DyInO_3$ crystals. The X-ray diffraction study unveils a Dy^{3+}-based buckled triangular lattice and a non-centrosymmetric space group $P6_3cm$, which is isostructural to previously reported hexagonal $REMnO_3$ and hexagonal $REInO_3$. Ferroelectricity and ferroelectric Z_3 vortex domains are demonstrated at room temperature, providing controllable vortex densities via different thermal histories. Anisotropic magnetization and thermodynamic measurement results imply the absence of long-range ordering down to 0.1 K, a broad feature in AC susceptibility around 0.9 K, and an effective S = 1/2 ground state of Dy^{3+} at low temperatures. Our findings suggest that $DyInO_3$ is a strongly entangled quantum magnet with the presence of geometric frustration and coherent structural topological defects.

2. Methods

$DyInO_3$ single crystal was grown by utilizing a laser floating zone technique. Dy_2O_3 (900 °C baked overnight) and In_2O_3 powders were mixed and sintered at 1400 °C for 20 h with one intermediate grinding. The sintered powder was pressed into a rod shape and sintered at 1400 °C for 10 h. Growth occurred under 8 atm oxygen pressure, with 10 rpm and 30 rpm rotations of the upper and lower shaft, respectively. The phase of the product strongly depends on feed rod stoichiometry and growth rate. A molar ratio of Dy_2O_3:In_2O_3 = 1:1.2 and 6 mm/h growth rate result in a mostly pure hexagonal phase crystal. The quality of *h*-DyInO3 was found to be well reproducible as long as the parameters mentioned above are strictly followed. Figure 1a displays a photograph of an as-grown *h*-$DyInO_3$ floating zone crystal.

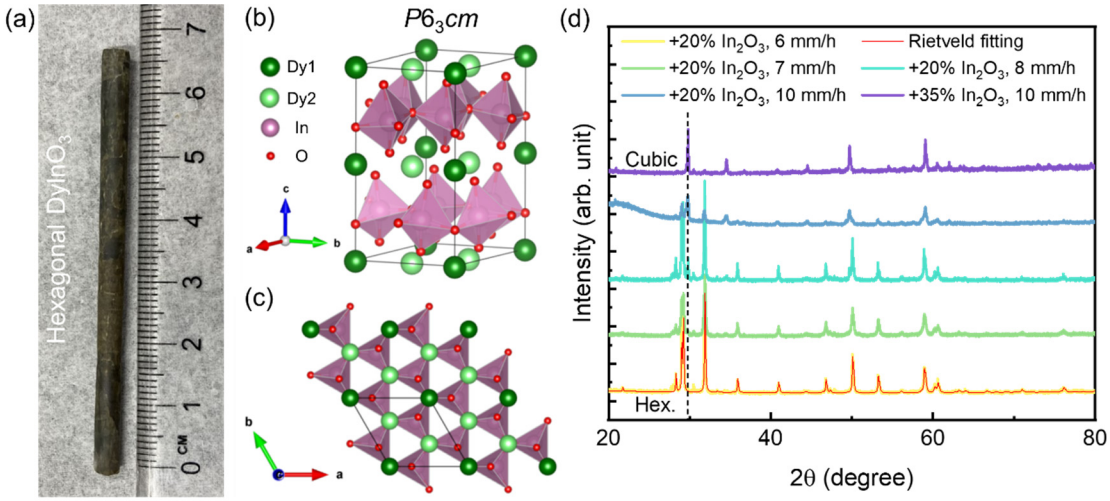

Figure 1. (**a**) A photograph of the floating zone crystal of hexagonal $DyInO_3$. (**b**) Crystal structure from refinement. (**c**) Top view of one layer. (**d**) Room temperature XRD patterns taken on crushed crystals grown using different In_2O_3 stoichiometry and the Rietveld fitting of the hexagonal phase.

Powder X-ray diffraction patterns of crushed crystals were collected in a Malvern Panalytical X'Pert diffractometer.

Chemical etching was carried out by heating a piece of crystal with a cleaved *ab* plane in concentrated H_3PO_4 at 150 °C for 30 min. The ferroelectric domain configuration was observed on the etched surface using an optical microscope. The ferroelectric hysteresis loop was measured using the "PUND" method provided in the Ferroelectric Material Test System (Radiant Technologies Inc., Albuquerque, NM, USA).

DC magnetic and heat capacity data were collected using Quantum Design MPMS and PPMS. A dilution refrigerator was used to collect AC magnetic data as low as 0.1 K.

3. Result and Discussion

3.1. Crystal Growth and Structure

Based on the previous study, $DyInO_3$ is almost located at the boundary of the hexagonal regime in the $REInO_3$ phase diagram [13]. Actually, the indate of the next rare earth element holmium, $HoInO_3$, irreversibly transforms into a cubic solid solution when sintered at higher than 1150 °C [14]. Therefore, one should expect that the crystal growth of $DyInO_3$ is difficult. One of the main difficulties in the floating zone growth of $DyInO_3$ is the significant evaporation loss of In_2O_3 from the molten zone, which produces In-deficient impurities. To overcome this difficulty, excessive In_2O_3 needs to be added to the feed rod in order to compensate for evaporation loss. On the other hand, residual In_2O_3 may also result in In-rich impurities if the quantity of excessive In_2O_3 in the feed rod exceeds evaporation loss. Therefore, the fine-tuning of the two key growth parameters, i.e., the quantity of excessive In_2O_3 and the growth rate, is essential for growing a high-quality $DyInO_3$ single crystal in the desired phase. Several combinations of these two parameters are examined, and the X-ray diffraction (XRD) patterns of the crushed products are shown in Figure 1d. The results indicate that the molar ratio of Dy_2O_3:In_2O_3 = 1:1.2 and 6 mm/h growth rate produce a $DyInO_3$ crystal in the target hexagonal phase (*h*-$DyInO_3$), and more excessive In_2O_3 and a slower growth rate cause increasing percentages of a cubic secondary phase, which is likely a Dy_2O_3-In_2O_3 solid solution. The Rietveld refinement of the hexagonal phase suggests a $P6_3cm$ space group (isostructural to other reported hexagonal $REInO_3$) and lattice parameters a = 6.3014(4) Å and c = 12.2977(1) Å. The crystallographic data and refined parameters are listed in Table 1. As shown in Figure 1b, the Dy^{3+} ions form a layered structure in between [InO_5] trigonal bipyramid blocks. Strictly speaking, each Dy^{3+} layer consists of two sorts of Dy^{3+} in different chemical environments, i.e., the Dy2 ions forming a honeycomb lattice and Dy1 ion stuffings at the center of each honeycomb. Considering that Dy1 and Dy2 have fairly close z coordinates, it can be concluded that Dy^{3+} ions form triangular layers with slight buckling.

Table 1. The structure parameters of *h*-$DyInO_3$ from powder X-ray diffraction performed at room temperature (290 K). Refined by $P6_3cm$ (No. 185), χ^2 = 2.54. Lattice parameters: a = 6.30144 Å and c = 12.29771 Å.

Atoms	*x*	*y*	*z*	*U*	Occ.	Site
Dy1	0	0	0.59481	0.001	1	2*a*
Dy2	0.33333	0.66667	0.56498	0.025	1	4*b*
In	0	0.34088	0.82774	0.012	1	6*c*
O1	0	0.27834	1.01379	−0.026	1	6*c*
O2	0	0.34201	0.66602	−0.025	1	6*c*
O3	0.33333	0.66667	0.34203	−0.015	1	4*b*
O4	0	0	0.28653	−0.03	1	2*a*

3.2. Room-Temperature Ferroelectricity

The point group of *h*-$DyInO_3$ (6*mm*) allows electric polarization along the c axis. In fact, ferroelectricity and Z_3 vortex ferroelectric domains have been reported in isostructural hexagonal $REInO_3$ such as $TbInO_3$ at room temperature [15]. Thus, one should expect room-temperature ferroelectricity in the *h*-$DyInO_3$ crystal as well.

Chemical etching is performed on a cleaved *ab* plane to search for ferroelectric domains. Ferroelectric domains with different polarization directions would show different depths on the surface after etching; thus, they can be visualized by an optical microscope. On an etched *h*-$DyInO_3$ surface, a typical Z_3 vortex domain pattern is observed (Figure 2a,b), and bright and dark intensity contrasts display ferroelectric domains with opposite polarizations. Additionally, a crystal cooled at 50 °C/h from 1400 °C (above the ferroelectric Curie temperature) shows a significantly higher vortex density than the 2 °C/h cooled crystal, which is consistent with the established Kibble–Zurek mechanism describing the evolution of topological defect density versus the cooling rate across the critical temperature [16].

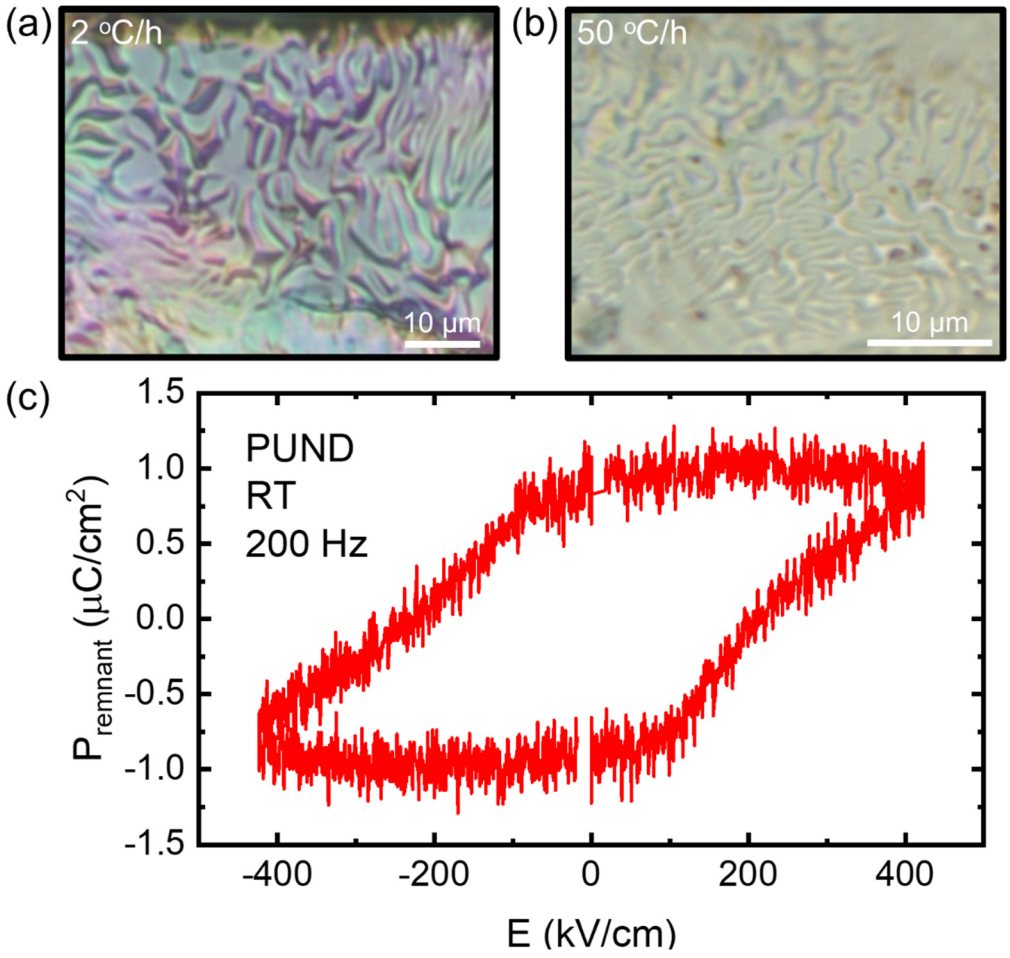

Figure 2. (**a**,**b**) Ferroelectric domain configuration of a 2 °C/h cooled crystal (**a**) and a 50 °C/h cooled crystal (**b**) revealed by chemical etching. (**c**) The P versus E hysteresis loop at room temperature measured using the PUND method.

As shown in Figure 2c, the room-temperature ferroelectricity of *h*-$DyInO_3$ is further confirmed by the polarization versus electric field (P-E) measurement, which provides a typical hysteresis loop at room temperature. The remnant polarization magnitude and coercive field are around 1 $\mu C/cm^2$ and 200 kV/cm, respectively, and these values are close to those observed in other hexagonal $REInO_3$. Considering the existence of Z_3 topological defects and the structural similarities with previously studied improper ferroelectrics $REMnO_3$, the observed ferroelectricity in *h*-$DyInO_3$ is likely an improper ferroelectricity induced by the trimerization of [InO_5] trigonal bipyramids [17].

3.3. Magnetic Property

Figure 3a displays the anisotropic susceptibility data (measured in 1000 Oe field) of an *h*-$DyInO_3$ single crystal as low as 1.8 K. No feature indicating a magnetic transition is observed, and it exhibits clear easy-plane anisotropy. The Curie–Weiss fitting of the susceptibilities in the high-temperature range (200 K to 300 K) produces μ_{eff} = 8.65 μ_B and T_{CW} = −31.4 K when the susceptibilities are parallel to *c* and μ_{eff} = 12.22 μ_B and T_{CW} = −22.4 K when the susceptibilities are perpendicular to *c*. The average of the high-temperature effective moments along two directions is close to the theoretical magnetic moment of a Dy^{3+} free ion: 10.48 μ_B. The Curie–Weiss fitting of the susceptibilities in the low-temperature range (5 K to 20 K) produces μ_{eff} = 4.96 μ_B and T_{CW} = −0.89 K when the susceptibilities are parallel to *c* and μ_{eff} = 11.54 μ_B and T_{CW} = −4.4 K when the susceptibilities are perpendicular to *c*. The reduction in the effective moment at low

temperatures is due to the evolution of the thermal population of crystal electric field (CEF) levels, and similar behaviors have been commonly found in rare-earth magnets [18]. Therefore, the magnetic parameters from the low-temperature fitting should describe the ground state of Dy^{3+} in *h*-$DyInO_3$ in a more precise manner. AC susceptibility versus temperature is measured as low as 0.1 K, and the data are shown in Figure 3b. A broad feature at 0.9 K with respect to AC susceptibility is observed, which may indicate spin freezing or a short-range magnetic correlation. Note that there is no significant chemical disorder in the *h*-$DyInO_3$ crystal based on the X-ray study. Therefore, the observed possible spin freezing may be related to ferroelectric domain interfaces and coherent Z_3 topological defects, which are unconventional cases. Another possible scenario is that spin freezing here is caused by spin frustration instead of structural defects, which has been reported in many geometrically frustrated magnets [19,20]. Consistent with the susceptibility data, isothermal magnetization versus magnetic field M(H) data at 1.8 K (Figure 3c) parallel to *c* and perpendicular to *c* exhibit a saturation tendency at around 2.9 μ_B and 8.5 μ_B, respectively, which exhibits easy-plane anisotropy. Interestingly, as shown in Figure 3d, the derivative of M(H) perpendicular to *c* shows a broad peak at around 1 T. This feature could be a CEF-level evolution, i.e., a change in CEF-level occupancies due to Zeeman splitting. At low temperatures and the zero field, the Dy^{3+} spin state is represented by the lowest CEF level, which is likely an S = 1/2 doublet because Dy^{3+} is a Kramer ion. Upon heating, the thermal excitation overcomes the energy gap between the ground state and excited states such that the spin state of Dy^{3+} gradually evolves into the free ion situation, which is experimentally evidenced by the broad peak in the magnetic heat capacity (Figure 4b) around 15 K, as well as the bending of the inverse susceptibility curve (Figure 3a) at that temperature. In a similar manner, applying the field introduces Zeeman energy, which could cause a CEF-level evolution as well. Note that the magnetic field of the anomaly in M(H) (~1 T) has a similar energy scale (estimated to be ~1 meV for Dy^{3+}), with the characteristic temperature of CEF-level evolution (~15 K) obtained from heat capacity and inverse susceptibility.

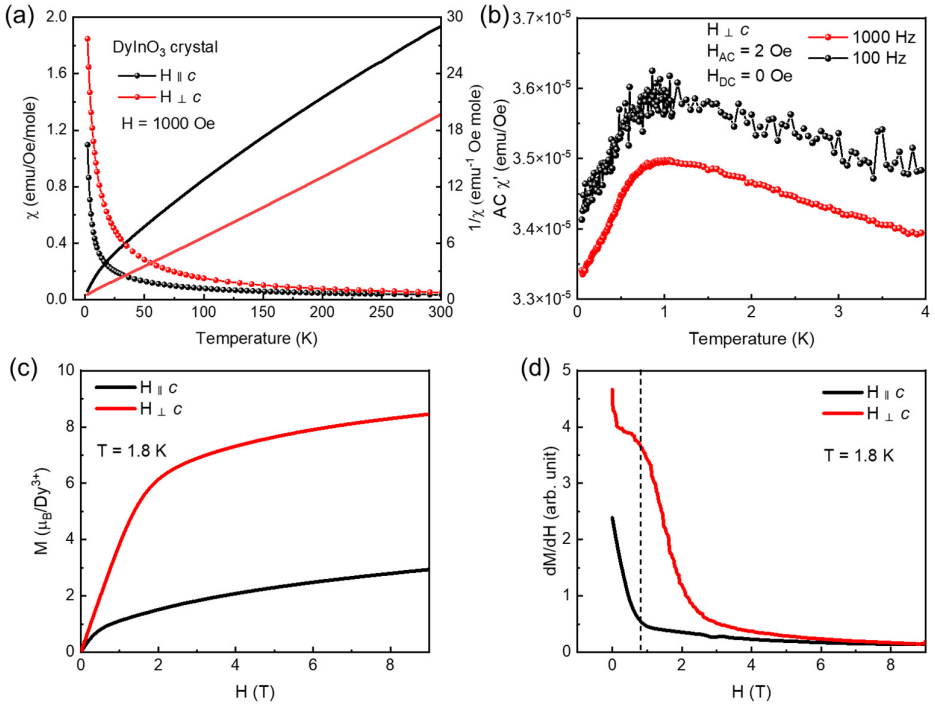

Figure 3. (**a**) DC magnetic susceptibility (solid lines with spheres) and inverse susceptibility versus temperature (solid lines) as low as 1.8 K. (**b**) AC magnetic susceptibility versus temperature as low as 0.1 K. (**c**) Magnetization versus field at 1.8 K. (**d**) Derivative magnetization versus field at 1.8 K. The vertical dashed line denotes the anomaly at around 1 T.

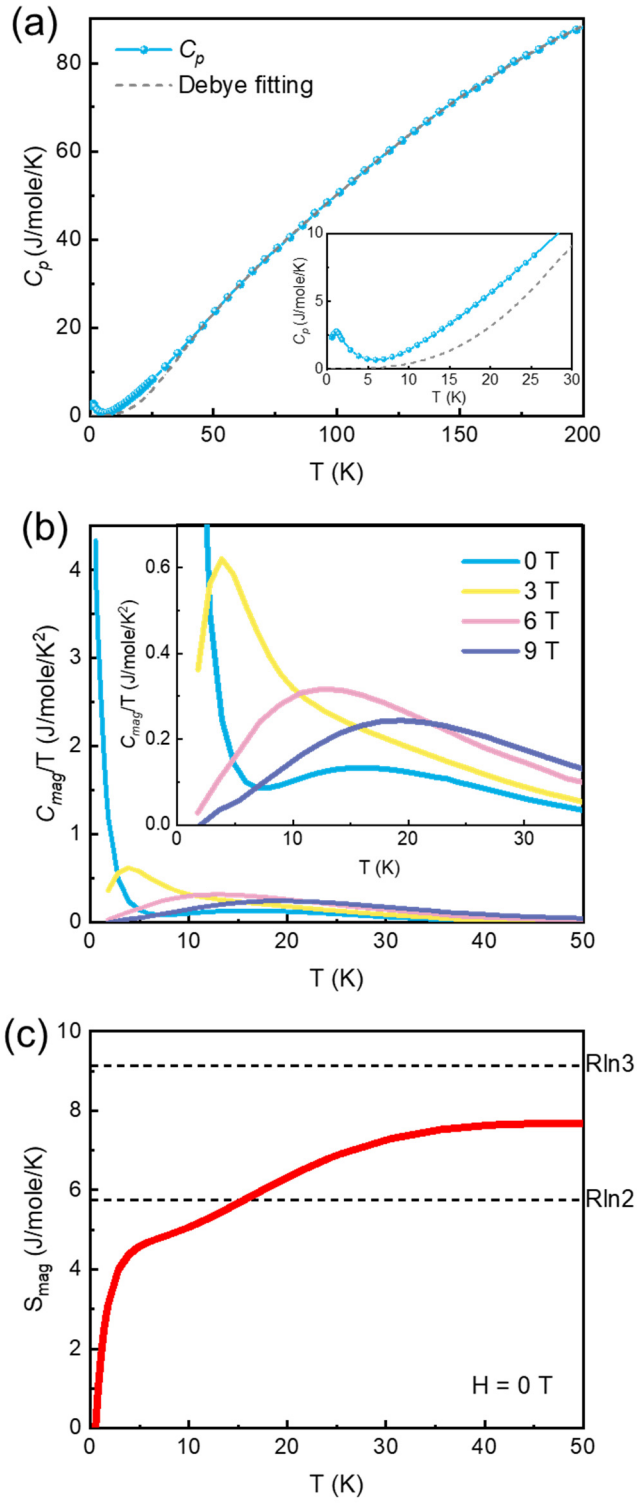

Figure 4. (**a**) Heat capacity and Debye fitting at 0 T. (**b**) Magnetic heat capacity over temperature as a function of temperature at 0 T, 3 T, 6 T, and 9 T. (**c**) Magnetic entropy as a function of temperature at 0 T. The horizontal dashed lines show theoretical magnetic entropy values of S = 1/2 (Rln2) and S = 1 (Rln3).

3.4. Thermodynamic Property

As shown in Figure 4a, the heat capacity (C_p) of *h*-$DyInO_3$ is measured from 0.5 K to 200 K in the zero magnetic field. The phonon contribution (C_{phonon}) should dominate the high-temperature heat capacity, and the data from 50 K to 200 K can be fitted well by using

a two-component Debye equation $C_{phonon} = 9R \sum_{n=1}^{2} C_n \left(\frac{T}{\Theta_{Dn}}\right)^3 \int_0^{\Theta_{Dn}/T} \frac{x^4 e^x}{(e^x-1)^2} dx$, where C_1 = 1.6, Θ_{D1} = 207(3) K, C_2 =3.4, and Θ_{D2} = 736(9) K. Below 50 K, the heat capacity starts to deviate from the phonon contribution, which indicates the onset of magnetic correlations, and the magnetic heat capacity (C_{mag}) can be obtained by $C_p - C_{phonon}$. A broad feature in C_p appears at around 0.9 K, which coincides with the observed feature in AC susceptibility (Figure 3b). However, no anomaly is observed in C_{mag}/T data in the zero field (Figure 4b), which suggests that the broad peak in C_p does not represent a magnetic ordering [21]. Instead, the zero-field C_{mag}/T shows a diverging tendency down to 0.5 K, which could be a Schottky anomaly due to the highly degenerate ground states, and it has been commonly observed in frustrated magnets [22]. As shown in the inset of Figure 4b, applying a magnetic field gradually shifts the Schottky anomaly peak in C_{mag}/T to a higher temperature, as expected. Finally, the magnetic entropy (S_{mag}) of Dy^{3+} is obtained by integrating C_{mag}/T over temperature, and the result is displayed in Figure 4c. At around 10 K, S_{mag} reaches a plateau with entropy around Rln2, and with elevated temperatures, S_{mag} starts to approach Rln3. Consistent with the scenario suggested by magnetic data, this behavior indicates a Dy^{3+} CEF-level evolution from the ground state to the second excited CEF level, and a similar transition has also been observed in the heat capacity of a rare-earth Yb_3Pt_4 magnet [23]. Therefore, the ground state of Dy^{3+} in *h*-$DyInO_3$ is likely a Kramer doublet. Although magnetization data demonstrate an easy-plane anisotropy, it is possible that the anisotropic *g* factors, instead of anisotropic magnetic exchange interactions, dominate magnetization anisotropy. Therefore, the easy-plane nature does not conflict with the effective S = 1/2 ground state in *h*-$DyInO_3$. Similar examples include $Na_2Co_2TeO_6$, in which the Co^{2+} ions are effective S = 1/2 at low temperatures, but the crystal exhibits easy-plane magnetic anisotropy [24,25].

4. Conclusions

In summary, we report the synthesis of a sizable $DyInO_3$ single crystal by utilizing the laser floating zone technique for the first time. The X-ray diffraction study reveals a non-centrosymmetric *P*63*cm* space group and Dy^{3+}-based triangular layers. Ferroelectricity and Z_3 vortex ferroelectric domains are demonstrated at room temperature. Magnetic and thermodynamic measurement results indicate frustrated antiferromagnetism and a possible effective S = 1/2 ground state of Dy^{3+}. Our findings suggest that $DyInO_3$ exhibits strong quantum spin entanglement co-existing with coherent structural topological defects. The sizable single crystal also provides excellent opportunities for the neutron study of CEF levels and exotic magnetic excitations in the future.

Author Contributions: Conceptualization, X.X. and S.-W.C.; Methodology, X.X. and C.W.; Writing—original draft, X.X.; Writing—review & editing, X.X., C.W. and S.-W.C.; Funding acquisition, S.-W.C. All authors have read and agreed to the published version of the manuscript.

Funding: The work at Rutgers University was supported by the DOE under Grant No. DOE: DE-FG02-07ER46382. The work at Pohang University of Science and Technology was supported by the National Research Foundation of Korea and funded by the Ministry of Science and ICT under Grant No. 2022M3H4A1A04074153 and 2020M3H4A2084417.

Data Availability Statement: The data that support the findings of this study are available from the authors upon reasonable request.

Conflicts of Interest: The authors declare no conflict of interest.

References

1. Goldschmidt, V.M. Die Gesetze der Krystallochemie. *Naturwissenschaften* **1926**, *14*, 477–485. [CrossRef]
2. Nordlander, J.; Anderson, M.A.; Brooks, C.M.; Holtz, M.E.; Mundy, J.A. Epitaxy of hexagonal ABO3 quantum materials. *Appl. Phys. Rev.* **2022**, *9*, 031309. [CrossRef]
3. Clark, L.; Sala, G.; Maharaj, D.D.; Stone, M.B.; Knight, K.S.; Telling, M.T.F.; Wang, X.; Xu, X.; Kim, J.; Li, Y.; et al. Two-dimensional spin liquid behaviour in the triangular-honeycomb antiferromagnet TbInO3. *Nat. Phys.* **2019**, *15*, 262. [CrossRef]

4. Kim, M.G.; Winn, B.; Chi, S.; Savici, A.T.; Rodriguez-Rivera, J.A.; Chen, W.C.; Xu, X.; Li, Y.; Kim, J.W.; Cheong, S.W.; et al. Spin-liquid-like state in pure and Mn-doped $TbInO_3$ with a nearly triangular lattice. *Phys. Rev. B* **2019**, *100*, 024405. [CrossRef]
5. Ye, M.; Xu, X.; Wang, X.; Kim, J.; Cheong, S.-W.; Blumberg, G. Crystal-field excitations and vibronic modes in the triangular-lattice spin-liquid candidate $TbInO_3$. *Phys. Rev. B* **2021**, *104*, 085102. [CrossRef]
6. Chae, S.C.; Lee, N.; Horibe, Y.; Tanimura, M.; Mori, S.; Gao, B.; Carr, S.; Cheong, S.W. Direct Observation of the Proliferation of Ferroelectric Loop Domains and Vortex-Antivortex Pairs. *Phys. Rev. Lett.* **2012**, *108*, 167603. [CrossRef]
7. Chae, S.C.; Horibe, Y.; Jeong, D.Y.; Rodan, S.; Lee, N.; Cheong, S.-W. Self-organization, condensation, and annihilation of topological vortices and antivortices in a multiferroic. *Proc. Natl. Acad. Sci. USA* **2010**, *107*, 21366–21370. [CrossRef]
8. Du, K.; Gao, B.; Wang, Y.; Xu, X.; Kim, J.; Hu, R.; Huang, F.-T.; Cheong, S.-W. Vortex ferroelectric domains, large-loop weak ferromagnetic domains, and their decoupling in hexagonal (Lu, Sc)FeO_3. *NPJ Quantum Mater.* **2018**, *3*, 33. [CrossRef]
9. Leiner, J.C.; Kim, T.; Park, K.; Oh, J.; Perring, T.G.; Walker, H.C.; Xu, X.; Wang, Y.; Cheong, S.W.; Park, J.-G. Magnetic excitations in the bulk multiferroic two-dimensional triangular lattice antiferromagnet (Lu,Sc)FeO_3. *Phys. Rev. B* **2018**, *98*, 134412. [CrossRef]
10. Wu, W.; Horibe, Y.; Lee, N.; Cheong, S.W.; Guest, J.R. Conduction of Topologically Protected Charged Ferroelectric Domain Walls. *Phys. Rev. Lett.* **2012**, *108*, 077203. [CrossRef]
11. Wu, X.; Petralanda, U.; Zheng, L.; Ren, Y.; Hu, R.; Cheong, S.-W.; Artyukhin, S.; Lai, K. Low-energy structural dynamics of ferroelectric domain walls in hexagonal rare-earth manganites. *Sci. Adv.* **2017**, *3*, e1602371. [CrossRef]
12. Kang, J.; Gao, Z.; Guo, C.; Zhu, W.; Huang, H.; Hong, J.; Cheong, S.-W.; Wang, X. A snapshot of domain evolution between topological vortex and stripe in ferroelectric hexagonal $ErMnO_3$. *J. Appl. Phys.* **2023**, *133*, 124102. [CrossRef]
13. Shukla, R.; Grover, V.; Srinivasu, K.; Paul, B.; Roy, A.; Gupta, R.; Tyagi, A.K. Rare earth indates (RE: La–Yb): Influence of the synthesis route and heat treatment on the crystal structure. *Dalton Trans.* **2018**, *47*, 6787–6799. [CrossRef]
14. Pistorius, C.W.F.T.; Kruger, G.J. Stability and structure of noncentrosymmetric hexagonal LnInO3 (Ln = Eu, Gd, Tb, Dy, Ho, Y). *J. Inorg. Nucl. Chem.* **1976**, *38*, 1471–1475. [CrossRef]
15. Kim, J.; Wang, X.; Huang, F.-T.; Wang, Y.; Fang, X.; Luo, X.; Li, Y.; Wu, M.; Mori, S.; Kwok, D.; et al. Spin Liquid State and Topological Structural Defects in Hexagonal $TbInO_3$. *Phys. Rev. X* **2019**, *9*, 031005. [CrossRef]
16. Lin, S.-Z.; Wang, X.; Kamiya, Y.; Chern, G.-W.; Fan, F.; Fan, D.; Casas, B.; Liu, Y.; Kiryukhin, V.; Zurek, W.H.; et al. Topological defects as relics of emergent continuous symmetry and Higgs condensation of disorder in ferroelectrics. *Nat. Phys.* **2014**, *10*, 970–977. [CrossRef]
17. Fennie, C.J.; Rabe, K.M. Ferroelectric transition in $YMnO_3$ from first principles. *Phys. Rev. B* **2005**, *72*, 100103. [CrossRef]
18. Xu, X.; Huang, F.-T.; Admasu, A.S.; Kim, J.; Wang, K.; Feng, E.; Cao, H.; Cheong, S.-W. Bilayer Square Lattice $Tb_2SrAl_2O_7$ with Structural Z8 Vortices and Magnetic Frustration. *Chem. Mater.* **2022**, *34*, 1225–1234. [CrossRef]
19. Booth, C.H.; Gardner, J.S.; Kwei, G.H.; Heffner, R.H.; Bridges, F.; Subramanian, M.A. Local lattice disorder in the geometrically frustrated spin-glass pyrochlore $Y_2Mo_2O_7$. *Phys. Rev. B* **2000**, *62*, R755–R758. [CrossRef]
20. Zhou, H.D.; Wiebe, C.R.; Harter, A.; Dalal, N.S.; Gardner, J.S. Unconventional spin glass behavior in the cubic pyrochlore $Mn_2Sb_2O_7$. *J. Phys. Condens. Matter* **2008**, *20*, 325201. [CrossRef]
21. Xu, X.; Cheng, G.; Ni, D.; Gui, X.; Xie, W.; Yao, N.; Cava, R.J. Spin disorder in a stacking polytype of a layered magnet. *Phys. Rev. Mater.* **2023**, *7*, 024407. [CrossRef]
22. Gao, B.; Chen, T.; Tam, D.W.; Huang, C.-L.; Sasmal, K.; Adroja, D.T.; Ye, F.; Cao, H.; Sala, G.; Stone, M.B.; et al. Experimental signatures of a three-dimensional quantum spin liquid in effective spin-1/2 $Ce_2Zr_2O_7$ pyrochlore. *Nat. Phys.* **2019**, *15*, 1052–1057. [CrossRef]
23. Bennett, M.; Khalifah, P.; Sokolov, D.; Gannon, W.; Yiu, Y.; Kim, M.; Henderson, C.; Aronson, M. A new unconventional antiferromagnet, Yb_3Pt_4. *J. Magn. Magn. Mater.* **2009**, *321*, 2021–2026. [CrossRef]
24. Lin, G.; Jeong, J.; Kim, C.; Wang, Y.; Huang, Q.; Masuda, T.; Asai, S.; Itoh, S.; Günther, G.; Russina, M.; et al. Field-induced quantum spin disordered state in spin-1/2 honeycomb magnet $Na_2Co_2TeO_6$. *Nat. Commun.* **2021**, *12*, 5559. [CrossRef] [PubMed]
25. Yao, W.; Li, Y. Ferrimagnetism and anisotropic phase tunability by magnetic fields in $Na_2Co_2TeO_6$. *Phys. Rev. B* **2020**, *101*, 085120. [CrossRef]